Geophysical Prospecting

EAGE EUROPEAN ASSOCIATION OF GEOSCIENTISTS & ENGINEERS

Geophysical Prospecting, 2015 doi: 10.1111/1365-2478.12232

Understanding the reverse time migration backscattering: noise or signal?

Esteban Díaz* and Paul Sava

Center for Wave Phenomena, Colorado School of Mines, Golden, CO 80401, USA

Received February 2014, revision accepted November 2014

ABSTRACT

Reverse time migration backscattered events are produced by the cross-correlation between waves reflected from sharp interfaces (e.g., salt bodies). These events, along with head waves and diving waves, produce the so-called *reverse time migration* artefacts, which are visible as low wavenumber energy on migrated images. Commonly, these events are seen as a drawback for the *reverse time migration* method because they obstruct the image of the geologic structure, which is the real objective for the process. In this paper, we perform numeric and theoretical analysis to understand the *reverse time migration* backscattering energy in conventional and extended images. We show that the *reverse time migration* backscattering contains a measure of the synchronization and focusing information between the source and receiver wavefields. We show that this synchronization and focusing information is sensitive to velocity errors; this implies that a correct velocity model produces reverse time migration backscattering with maximum energy. Therefore, before filtering the reverse time migration backscattered energy, we should try to obtain a model that maximizes it.

INTRODUCTION

Reverse time migration (RTM) is not a new imaging technique (Baysal, Kosloff, and Sherwood 1983; Whitmore 1983; McMechan 1983). However, it was not until the late 1990s and mainly the 2000s that computational advances allowed the geophysical community to use this technology for exploratory 3D surveys. In general and especially in complex geological settings, RTM produces better images than other methods. Imaging methods such as Kirchhoff migration and one-way equation migration are based on approximate solutions to the wave equation. Kirchhoff migration, a high-frequency asymptotic solution to the wave equation, becomes *inaccurate* for complex velocity models. This technique also fails to handle multipathing and typically creates the images based on a single travel-time arrival (e.g., most energetic or first arrival). Other methods based on approximations to the wave equation, such as phase-shift migration (Gazdag 1978), rely on a v(z) earth model, and further approximations are needed to account for lateral variations (Gazdag and Sguazzero 1984). In addition to earth model considerations, one-way wave equation migration *propagates* the wavefields in either the upward or the downward direction; this approximation becomes inexact when the waves propagate horizontally. Therefore, this technique fails to properly handle overturning waves and reflections from steep-dip structures. RTM's propagation engine, a two-way wave equation, makes this imaging method robust and accurate because it honors the kinematics of the wave phenomena by allowing waves to propagate in all directions regardless of the velocity model or the direction of propagation. This method also takes into account, in a natural way, multipathing and reflections from steep dips.

A striking characteristic of RTM is the presence of low wavenumber events in the image that are uncorrelated with the geology. The two-way wave equation simulates scattered waves in all directions. Therefore, the imaging condition produces new events not observed in other imaging methods that

*E-mail: ediazpan@mines.edu

© 2015 European Association of Geoscientists & Engineers

correspond to the cross-correlation between diving waves, head waves, and backscattered waves. The cross-correlation between the backscattered waves is more visible in the presence of sharp boundaries (e.g., the top of salt), which produces strong events that mask the image of the earth reflectivity above the salt. The backscattered events are considered as noise and are normally filtered in order to get the image of earth reflectivity.

The seismic industry has dedicated effort and time developing algorithms and strategies to filter out the backscattered energy from the image. We can classify the filtering approaches in two general families: pre-imaging condition and post-imaging condition.

The pre-imaging condition family modifies the wavefields (either by modeling or wavefield decomposition) in such a way that the backscattered events do not form during the imaging process. One strategy in the pre-imaging condition category is wavefield decomposition (Liu *et al.* 2011; Fei, Luo, and Schuster 2010). In this method, the source and receiver wavefields are decomposed in upgoing and downgoing directions. In the imaging step, we cross-correlate only the wavefields that propagate in opposite directions, producing an image that corresponds to the geology. The cross-correlation between wavefields travelling in parallel directions is discarded because *it produces* events that obstruct the geology. Other pre-imaging condition approaches are performed by modifying the wave equation to attenuate the reflections coming from sharp interfaces (Fletcher *et al.* 2005). A similar method applicable to post-stack migration uses impedance matching at sharp interfaces (Baysal, Kosloff, and Sherwood 1984).

In the post-imaging family, the artefacts are attenuated by filtering. These filtering approaches are considerably cheaper because they operate in the image space and not on the wavefields. A straightforward approach is to apply a Laplacian operator to the image (Youn and Zhou 2001); this operator acts as a high-pass filter and is effective because the backscattered events have a strong low wavenumber component. A second strategy is a signal/noise separation by least squares filtering. In this case the signal is defined as the reflectivity and the noise is the backscattered energy (Guitton, Kaelin, and Biondi 2007). Finally, extended imaging conditions (Rickett and Sava 2002; Sava and Fomel 2006; Sava and Vasconcelos 2011) provide information about the wavefield similarity for different space and/or time lags and can also be used to discriminate the backscattered energy. Kaelin and Carvajal (2011) take advantage of the way backscattered events appear in time-lag gathers. The backscattered events map toward zero time lag when a correct velocity model is used for imaging, whereas the primary reflections map within a limited slope range constrained by the velocity model. This difference in slope allows us to design 2D filters that preserve events within the primary reflections' range and attenuate the backscattered energy.

In this article we analyse the information carried by the backscattered energy in the extended images. We show that the backscattered waves provide important information about the synchronization between the reconstructed wavefields in the subsurface, i.e., an image obtained with a correct velocity model shows maximum backscattered energy. The presence of backscattered energy in the image depends not only on the interpretation of the sharp interface but also on the velocity above it. We analyse the mapping patterns of the backscattered events in the extended images using wavefield decomposition approaches and conclude that backscattered energy is sensitive to the velocity model accuracy and therefore should be included as a source of information to migration velocity analysis (MVA). Contrary to common practice, we assert that backscattering artefacts should be enhanced during RTM to constrain the velocity models, and they should only be removed in the last stage of imaging.

WAVE EQUATION IMAGING CONDITIONS

Conventional imaging condition

The conventional imaging condition (Claerbout 1985) is a zero time-lag cross-correlation between the source wavefield and the receiver wavefields:

$$R(\mathbf{x}) = \sum_{shots} \sum_{t} u_s(\mathbf{x}, t) u_r(\mathbf{x}, t), \tag{1}$$

which honors the single scattering or Born assumption. Under this assumption the forward scattered source wavefield generates secondary waves as it interacts with the medium discontinuities. These secondary waves propagate in space and are recorded at the surface. This assumption means that both the source and receiver wavefields carry only transmitted energy through interfaces between layers with different elastic properties.

A wavefield extrapolated with RTM could show, depending on the complexity of the geology, waves travelling in both upward and downward directions, such as diving waves, head waves, and backscattered waves. The interaction between these waves contained in the source and receiver wavefields generates new events in the image that are commonly referred to as artefacts because they do not follow the geology (i.e., earth reflectivity), which is the objective of the imaging process. The correlation between forward and

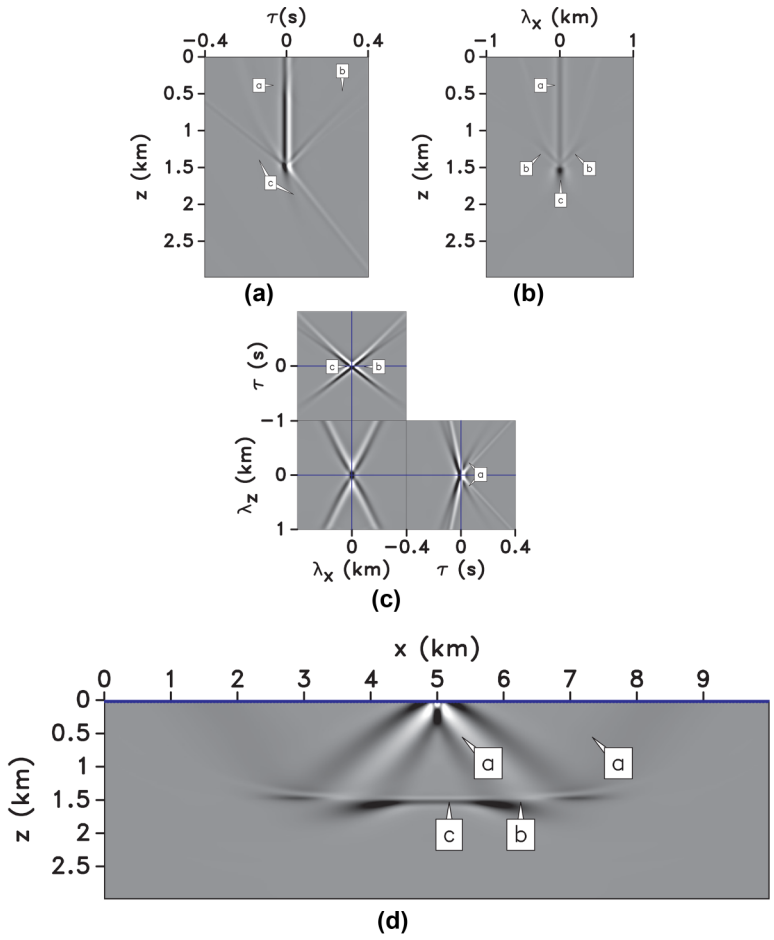


Figure 1 Synthetic model example: (a) time-lag gather at x = 5 km; (b) space-lag gather at x = 5 km; (c) CIP at x = 5 km, z = 1.5 km; and (d) migrated image of one shot (in x = 5 km, z = 0 km) with receivers in the surface.

backscattered waves is particularly strong when sharp boundaries are present in the velocity model (e.g., salt bodies).

If a sharp boundary is present in the model, we can decompose the source wavefield into forward scattered and backscattered energy that originates at the sharp boundary:

$$u_s(\mathbf{x}, t) = u_s^b(\mathbf{x}, t) + u_s^f(\mathbf{x}, t), \tag{2}$$

where superscripts ^{b} and ^{f} stand for backscattered and forward scattered wavefields, respectively. The same idea can be applied to the receiver wavefield:

$$u_r(\mathbf{x}, t) = u_r^b(\mathbf{x}, t) + u_r^f(\mathbf{x}, t). \tag{3}$$

It is not clear how to split the wavefields in backscattered and forward components. Fei *et al.* (2010) and Liu *et al.* (2011) propose a splitting based on up/down separation. This separation based on slope is effective in simple geological settings where the bedding is mostly horizontal.

By taking advantage of the linearity of equation (1), we can split the conventional imaging condition as follows:

$$R(\mathbf{x}) = R^{ff}(\mathbf{x}) + R^{bb}(\mathbf{x}) + R^{bf}(\mathbf{x}) + R^{fb}(\mathbf{x}). \tag{4}$$

Here, the first superscript is associated with the source wavefield, and the second is associated to the receiver wavefield. For example, $R^{fb}(\mathbf{x})$ is an image constructed with the forward scattered source wavefield and the backscattered receiver wavefield.

By analyzing the individual contributions to the image, we can better understand how the backscattered events are constructed in the image. This analysis is similar to the one of Fei *et al.* (2010) and Liu *et al.* (2011) whose objective is to filter out the non-geological portions of the image. Here, we approach the problem in a broader sense by attempting to understand the physical meaning of the backscattered energy and its uses for velocity model building.

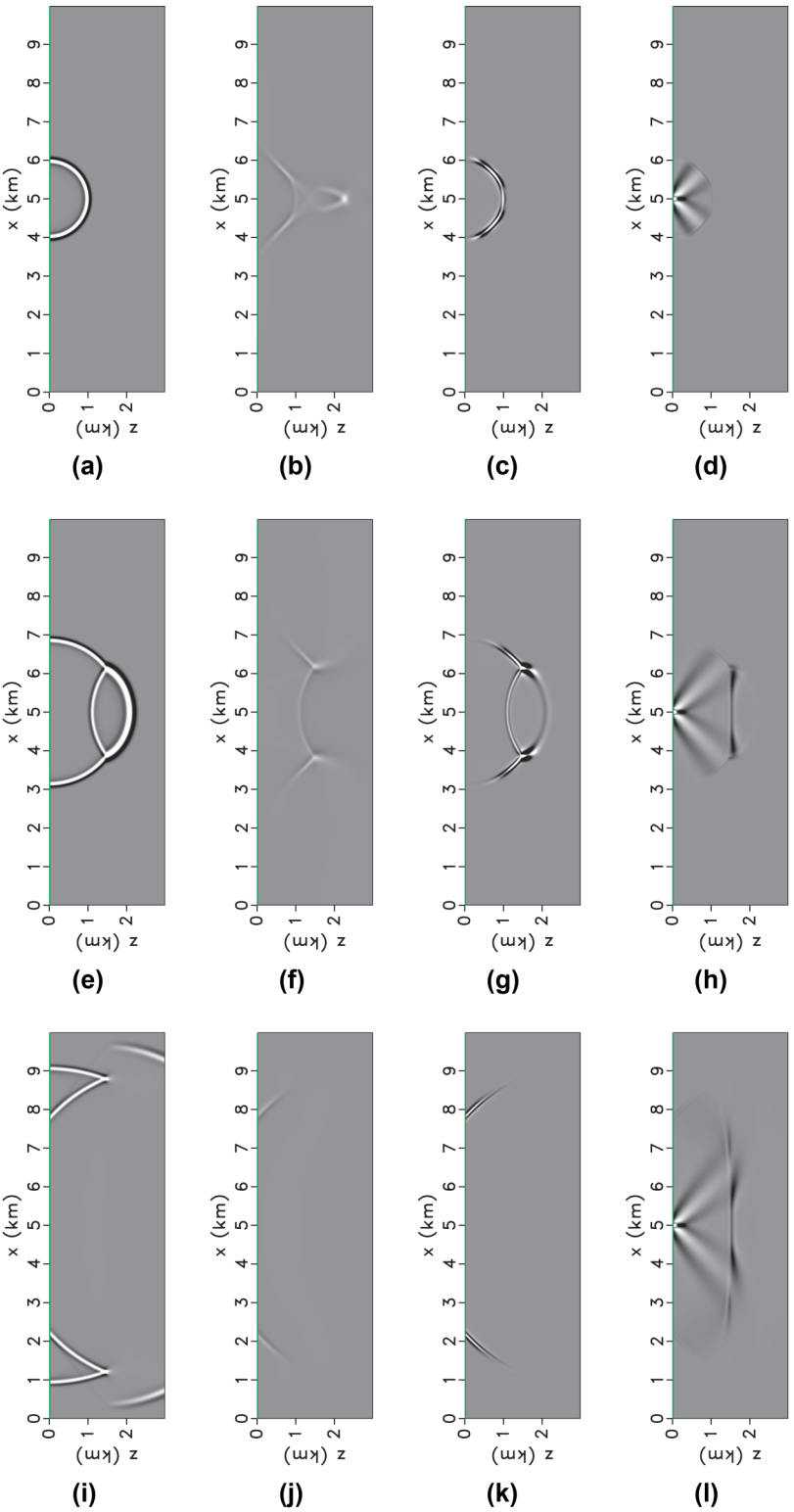


Figure 2 Pictorial explanation of RTM imaging: rows 1, 2, and 3 correspond to three different snapshots at times $t_1 = 0.150$ second, $t_2 = 0.275$ second and $t_3 = 0.500$ second. Columns 1 to 4 correspond to the source wavefield, the receiver wavefield, the multiplication of the source and receiver wavefields, and the accumulated image over time, respectively.

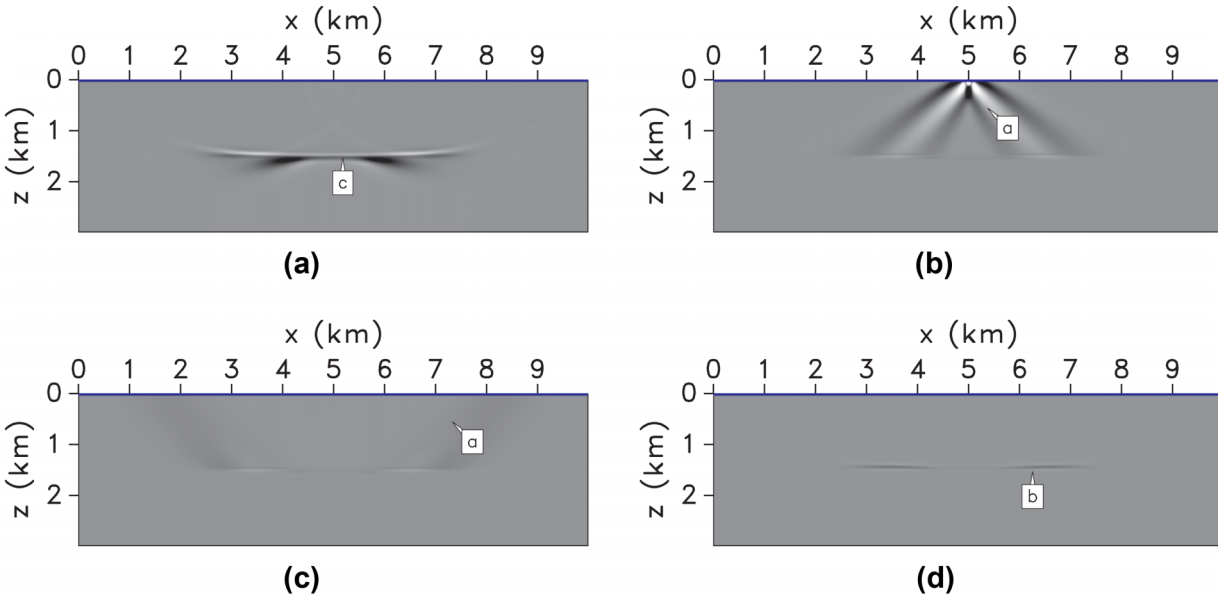


Figure 3 Illustration of the linearity of the conventional imaging condition. We can split the conventional image (Figure 1d) in four separate images, (a) $R^{ff}(\mathbf{x})$, (b) $R^{fb}(\mathbf{x})$, (c) $R^{fb}(\mathbf{x})$, and (d) $R^{bb}(\mathbf{x})$, corresponding to the correlation of the forward scattered and/or backscattered components of the source and receiver wavefields.

Backscattered events in the conventional image

In order to gain an understanding of the RTM backscattered events, we use a simple model with two layers and strong velocity contrast. Figure 1d shows the image obtained with the conventional imaging condition for one shot at $x = 5$ km. This image has strong backscattered energy, indicated with letter "a", above the reflector located at $z = 1.5$ km.

To better understand the origin of the backscattered artefacts, we illustrate the wavefields used for imaging our simple model. Figures 2a, 2e, and 2i show three different snapshots of the source wavefield. Likewise, Figs. 2b, 2f, and 2j show the same snapshots for the receiver wavefield. Figures 2c, 2g, and 2k show the product between the source and receiver wavefields for the same time snapshots. Finally, Figs. 2d, 2h, and 2l show the accumulated image as a function of time (integration over time of the product between wavefields).

Figure 2d shows the interaction between the forward scattered source wavefield u_s^f, shown in Fig. 2a, and the backscattered receiver wavefield u_r^b, shown in Fig. 2b. In this case, the backscattered receiver wavefield travels in perfect synchronization with the forward scattered source wavefield; therefore their product, shown in Fig. 2c, stacks coherently in the imaging process, generating the $R^{fb}(\mathbf{x})$ contribution to the image $R(\mathbf{x})$. In the $R^{fb}(\mathbf{x})$ image, the backscattered receiver wavefield behaves as the forward scattered source wavefield, which is the reason why the backscattered energy is imaged toward the source location. In the partial image at $t = 0.275$ second, shown in Fig. 2h, we see how *the reflector image arises*. The backscattered source wavefield, shown in Fig. 2e, generates new backscattered events corresponding to the $R^{bf}(\mathbf{x})$ image. In the snapshot at $t = 0.5$ second, the reflector is completely imaged, and for the remaining time, we only add backscattered energy corresponding to the $R^{bf}(\mathbf{x})$ image. Here, the backscattered source wavefield behaves as the receiver wavefield, and its energy maps toward the receivers. We can see that, after the imaging process is finished (Figure 1d) the backscattered energy is maximum near the critical angle range (where the reflected source and receiver wavefields have maximum energy).

Using wavefield decomposition allows isolating the individual contributions of equation (4). Figure 3a shows the cross-correlation between forward scattered wavefields, producing an image due to the earth reflectivity. Figures 3b and 3c show the images $R^{fb}(\mathbf{x})$ and $R^{bf}(\mathbf{x})$ corresponding to the backscattered energy, which maps toward the source and the receivers, respectively. The image corresponding to the $R^{bb}(\mathbf{x})$, shown in Fig. 3d, contains additional contribution to the reflectivity of the earth due to the cross-correlation between reflected wavefields. Fei *et al.* (2010) take advantage of this analysis to define an image free from backscattered energy as $R(\mathbf{x}) = R^{ff}(\mathbf{x}) + R^{bb}(\mathbf{x})$. Here, we want to better understand

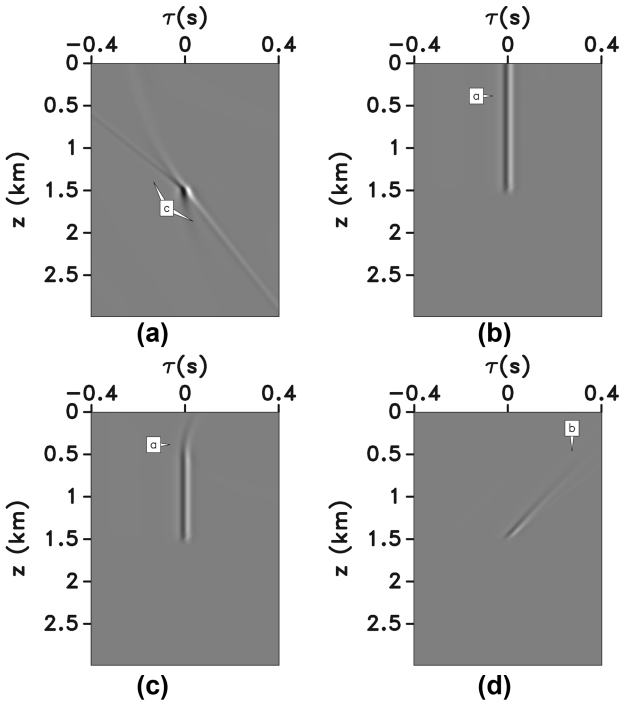


Figure 4 Illustration of the linearity of the time-lag extended imaging condition. We can split a time-lag gather (Fig. 1 a) in four separate images, (a) $R^{ff}(z,\tau)$, (b) $R^{bf}(z,\tau)$, (c) $R^{fb}(z,\tau)$ and (d) $R^{bb}(z,\tau)$, corresponding to the forward scattered and/or backscattered components of the source and receiver wavefields.

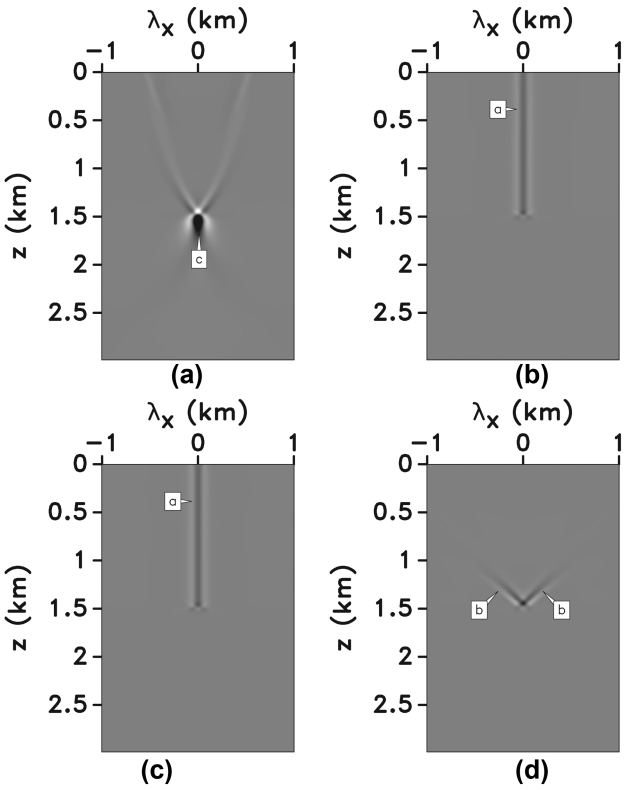


Figure 5 Illustration of the linearity of the space-lag extended imaging condition. We can divide Fig. 1b in four images, (a) $R^{ff}(z,\lambda_x)$, (b) $R^{bf}(z,\lambda_x)$, (c) $R^{fb}(z,\lambda_x)$, and (d) $R^{bb}(z,\lambda_x)$, corresponding to the correlation of the forward scattered and/or backscattered components of the source and receiver wavefields.

the meaning and uses of the other two partial images $R^{fb}(\mathbf{x})$ and $R^{bf}(\mathbf{x})$.

Extended imaging condition

The extended imaging condition (Rickett and Sava 2002; Sava and Fomel 2006; Sava and Vasconcelos 2011) is similar to the conventional imaging condition, except the cross-correlation lags between source and receiver wavefields are preserved in the output:

$$R(\mathbf{x},\boldsymbol{\lambda},\tau)=\sum_{shots}\sum_{t}u_s(\mathbf{x}-\boldsymbol{\lambda},t-\tau)u_r(\mathbf{x}+\boldsymbol{\lambda},t+\tau). \qquad (5)$$

Here $\boldsymbol{\lambda}$ and τ represent the space lags and time lags, respectively, of the cross-correlation. The conventional image is a special case of the extended image $R(\mathbf{x})=R(\mathbf{x},\mathbf{0},0)$.

Using extended images allows measuring the accuracy of the velocity model by analyzing the moveout of the events (Yang and Sava 2010), and we can perform transformations from the extended to the angle domain (Sava and Fomel 2003, 2006; Sava and Vlad 2011). The extended images provide a measurement of the similarity between the source and receiver wavefields along space and time; hence, we can exploit these images to analyse and better understand the RTM backscattered events.

In equation (5), we observe an increase in the dimensionality of the image, from three to seven dimensions, if we decide to extend the image in all directions. It is common to perform the analysis of extended images at limited locations in order to make this methodology feasible for large datasets. For cost considerations, we often use an extension for common image gathers (CIGs), for instance, the time-lag axis (τ) or the space-lag axis (λ_x). We can also consider common image point (CIP) gathers, where we fix an observation point $\mathbf{c}=(x,y,z)$ and analyse the image as a function of extensions $\boldsymbol{\lambda},\tau$. If the dip is known, not all the space extensions, $\boldsymbol{\lambda}$, are needed.

Figures 1a to 1c show a time-lag gather, a space-lag gather, and a CIP, respectively, which represent subsets at fixed surface positions (for CIGs) or fixed space positions (for

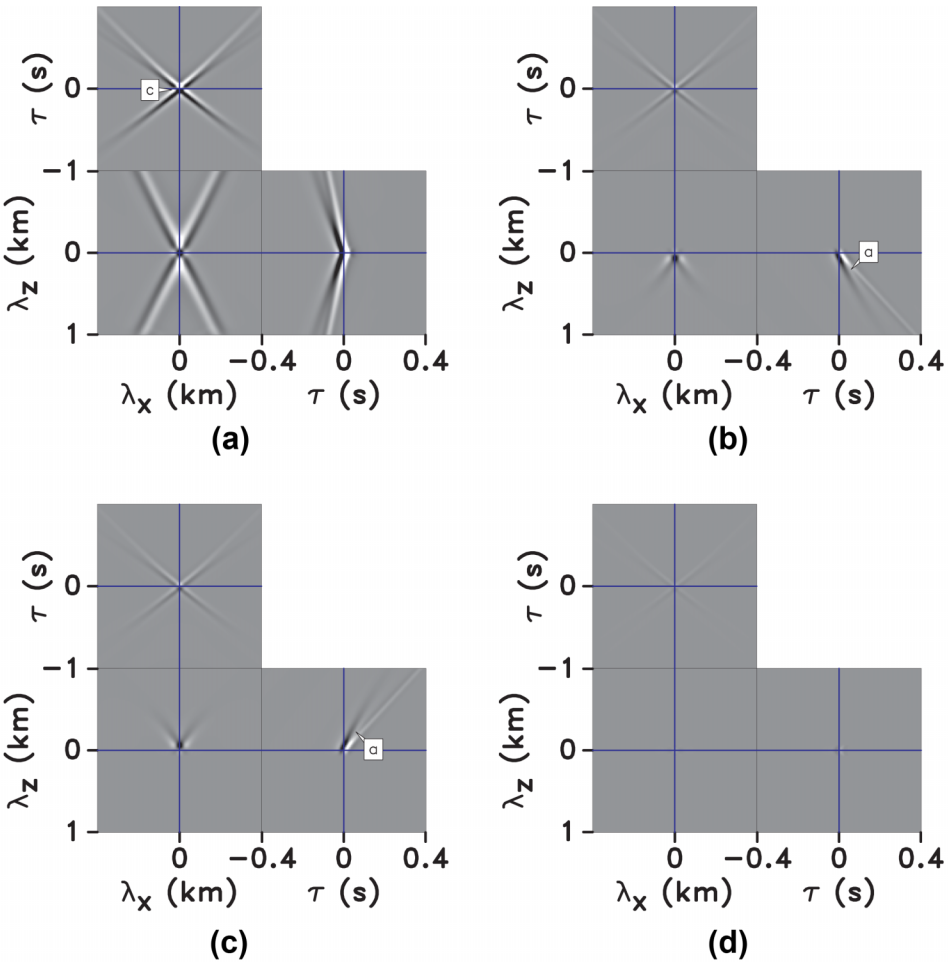


Figure 6 Illustration of the linearity of the extended imaging condition for a CIP. We can decompose a CIP (Fig. 1c) in four images (a) $R^{ff}(\boldsymbol{\lambda}, \tau)$, (b) $R^{bf}(\boldsymbol{\lambda}, \tau)$, (c) $R^{fb}(\boldsymbol{\lambda}, \tau)$, (d) $R^{bb}(\boldsymbol{\lambda}, \tau)$, corresponding to the correlation between the forward scattered and/or backscattered components of the source and receiver wavefields.

CIPs). Despite the fact that our model has only one reflector, we can identify several events in the conventional and extended images. Letter "a" indicates backscattered events (produced by the correlation of wavefields travelling in the same direction), letter "b" indicates the events produced by the cross-correlation of reflected wavefields, and letter "c" indicates the cross-correlation between forward scattered wavefields.

In the presence of sharp velocity interfaces, we can use the concept of equation (4) and construct four partial extended images:

$$R(\mathbf{x}, \boldsymbol{\lambda}, \tau) = R^{ff}(\mathbf{x}, \boldsymbol{\lambda}, \tau) + R^{bb}(\mathbf{x}, \boldsymbol{\lambda}, \tau) + R^{fb}(\mathbf{x}, \boldsymbol{\lambda}, \tau) + R^{bf}(\mathbf{x}, \boldsymbol{\lambda}, \tau). \quad (6)$$

Time-lag common image gathers

Using equation (6), we analyse the individual contributions for the time-lag gather shown in Fig. 1a. Figure 4a shows the image $R^{ff}(z, \tau)$ with a change in the slope of the events due to the abrupt velocity variation of the model. Above the reflector depth, the slope is controlled by the velocity of layer 1, whereas below the interface, the slope is controlled by the velocity of layer 2. Figures 4c and 4b show the backscattered event contributions $R^{fb}(z, \tau)$ and $R^{bf}(z, \tau)$, respectively, which indicate that the backscattered event maps towards $\tau=0$ in the extended image. This means that we only get a contribution when we do not dislocate the wavefields by shifting them in time, thus reinforcing the idea of wavefield synchronization. Figure 4d shows the $R^{bb}(z, \tau)$ image; in this case,

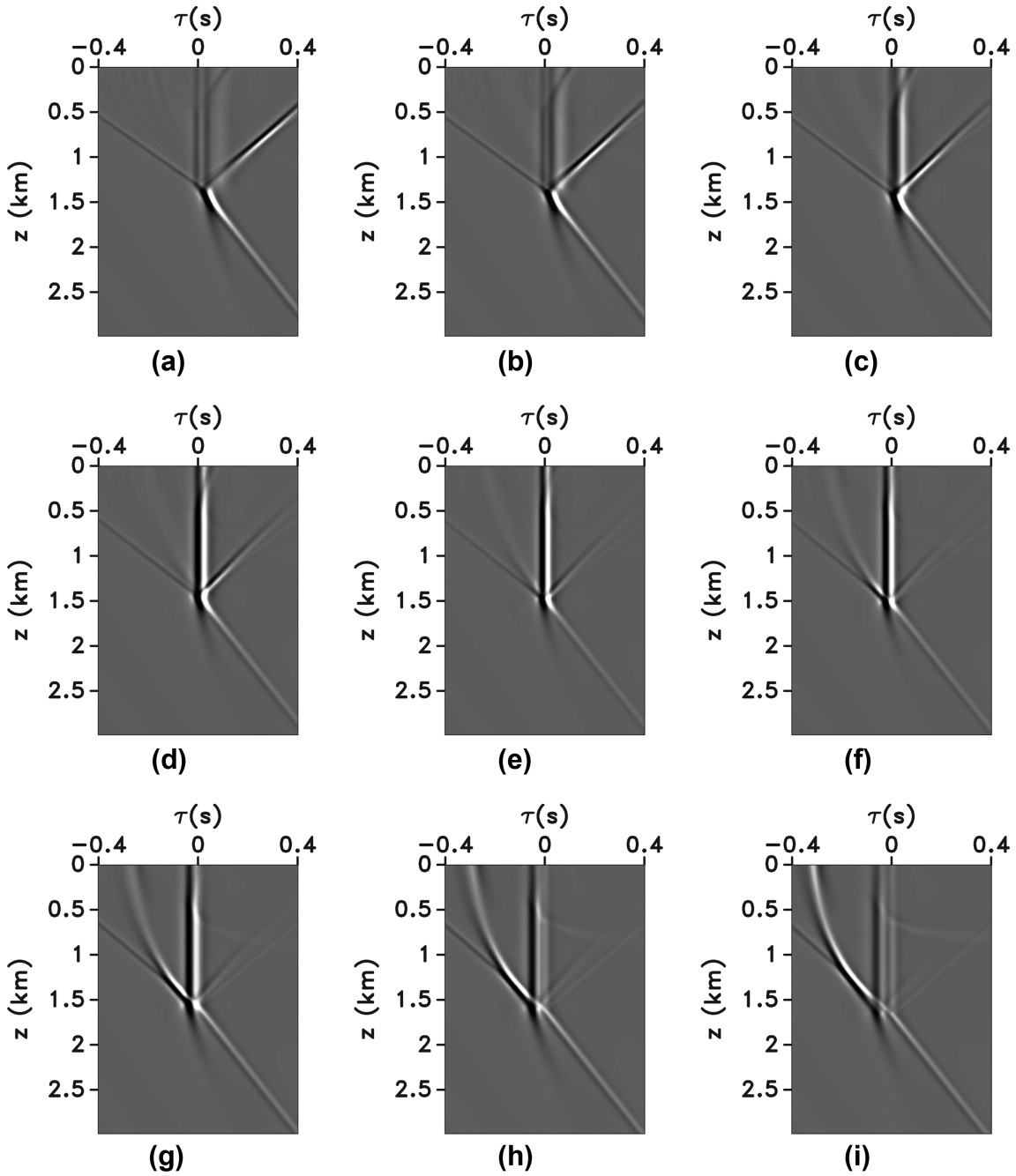


Figure 7 Model error sensitivity with time-lag gathers: (a) −12%, (b) −9%, (c) −6%, d) −3%, (e) 0%, (f) +3%, (g) +6%, (h) +9%, and (i) +12% velocity perturbation in the top layer. The maximum energy of the backscattered events occurs with correct velocity shown in panel (e).

the source wavefield is going in the upward direction and the receiver wavefield is going in the downward direction, which is as if we change the order of cross-correlation in equation (5). This is why these events map in the time-lag gathers with a slope opposite to the primary above the interface. Because the reflected waves only travel in the upper layer, we observe this image above the reflector. In the $R^{bb}(z, \tau)$ image, we see two events that map with similar slope: one has the exact opposite slope as the one shown by the primary reflection, and the other has a slightly higher slope (therefore indicating faster velocity) and corresponds to the interaction between head waves produced by the velocity discontinuity and the

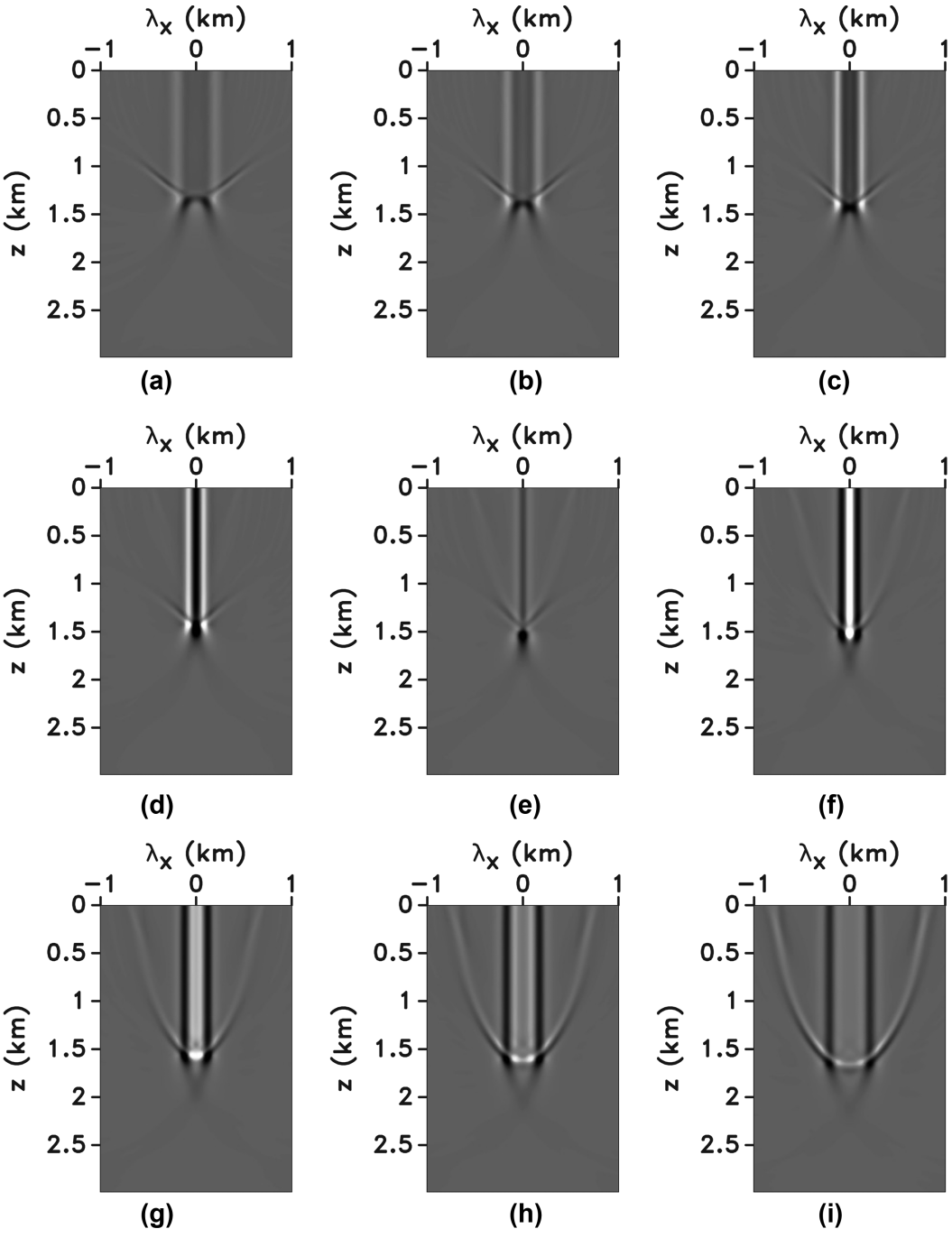


Figure 8 Model error sensitivity with time-lag gathers: (a) −12%, (b) −9%, (c) −6%, (d) −3%, (e) 0%, (f) +3%, (g) +6%, (h) +9%, and (i) +12% velocity perturbation in the top layer. The maximum energy of the backscattered events occurs with correct velocity shown in panel (e).

reflected wavefields. In the time-lag gathers, the slope of the primaries is very different from the backscattered events slope. Kaelin and Carvajal (2011) use the slope difference to filter the backscattered events in this domain and to extract the conventional image from the filtered extended image $R(\mathbf{x}) = R(\mathbf{x}, \tau = 0)$.

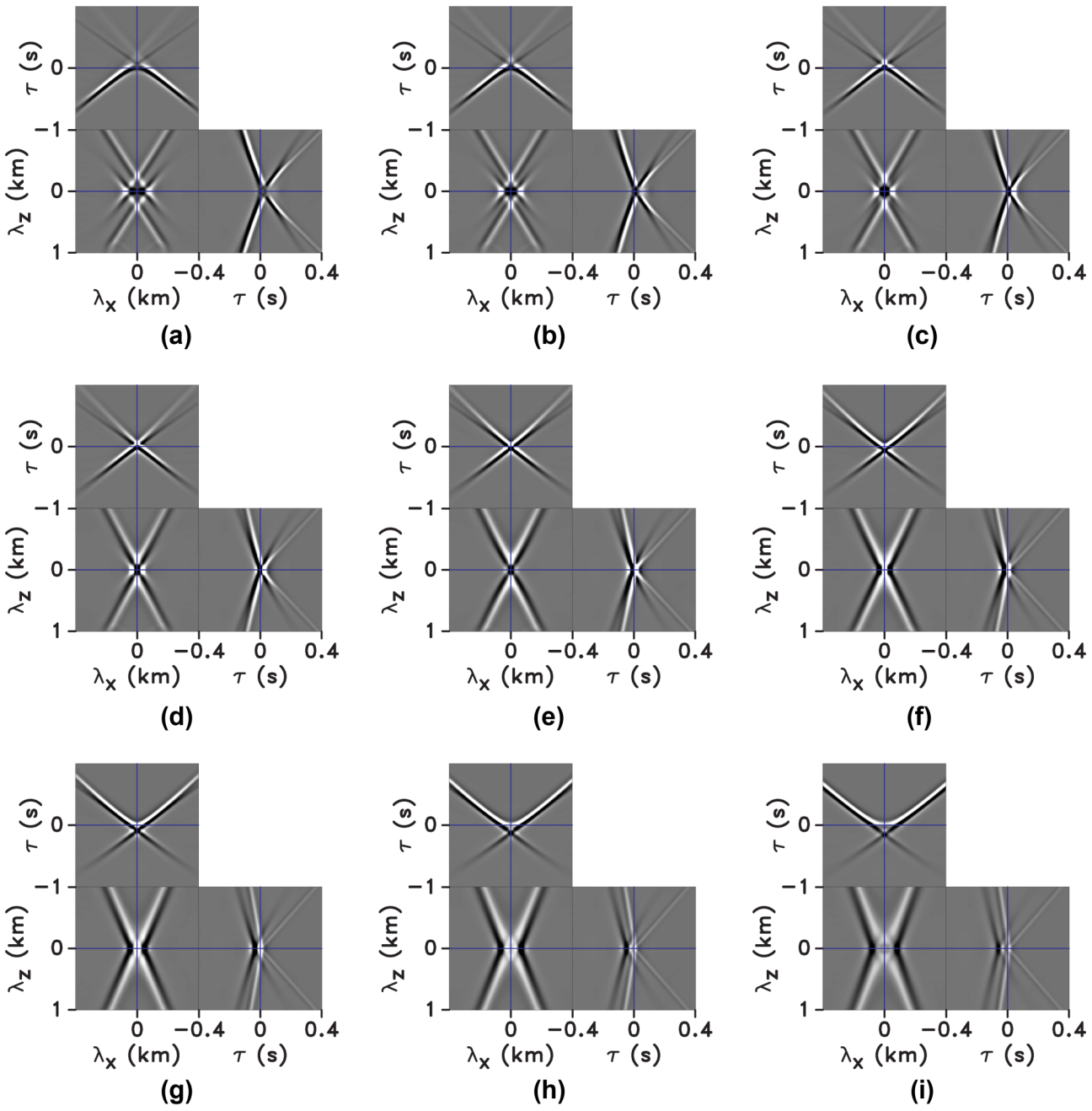


Figure 9 Model error sensitivity with CIP gathers: (a) −12%, (b) −9%, (c) −6%, (d) −3%, (e) +0%, (f) +3%, (g) +6%, (h) +9%, and (i) +12% velocity perturbation in the top layer.

Space-lag common image gathers

Figure 1b shows a space-lag gather for the various combinations of the source and receiver wavefield components. We note that, with the correct velocity model, both primaries and backscattered events map to $\lambda_x = 0$ since the velocity used for imaging is correct. Figure 5a shows the $R^{ff}(z, \lambda_x)$ image with the energy correctly focused at $\lambda_x = 0$. Figures 5b and 5c show the backscattered events $R^{bf}(z, \lambda_x)$ and $R^{fb}(z, \lambda_x)$ in the space-lag gathers, which also map toward $\lambda_x = 0$. Figure 5d shows the image coming from the reflected wavefields $R^{bb}(z, \lambda_x)$; in this case, the events are visible only above the reflector because the waves travel only in the first layer.

Common-image point gathers

The events involving backscattered energy are also visible in CIP gathers. Figure 1c shows a CIP extracted at $\mathbf{c} = (5, 1.5)$ km. Figure 6a shows the CIP for the forward scattered wavefields $R^{ff}(\mathbf{x}, \lambda, \tau)$. The energy focuses at zero lag for the $\tau - \lambda_x$ panel. The $\lambda_z - \tau$ shows a kink produced by the abrupt change in velocity for the primaries, which are mapped at negative τ. Figure 6c shows the $R^{fb}(\mathbf{x}, \boldsymbol{\lambda}, \tau)$ image, and we can see a change in the $\lambda_z - \tau$ plane, where the backscattered energy is mapped to positive lags. Figure 6b shows the complementary backscattered energy that is mapped to negative λ_z and positive τ lags. The CIP from the reflected wavefields (Figure 6d) shows weak energy concentrated at zero lags.

Sensitivity to velocity errors

In the previous sections we have explained the concept of wavefield synchronization for correct velocity, which implies that, for correct velocity, the backscattered energy maps toward zero lags. Here, we analyse the behavior of backscattered events in the presence of velocity errors. We test the sensitivity of the backscattered events with the same synthetic data discussed previously. In this case, we construct the images with different models characterized by a constant error varying from -12% to $+12\%$ in layer 1. We keep the interface consistent with the velocity used for imaging, i.e., we assume that the interface producing backscattered energy is placed in the model according to the velocity in layer 1. Fig. 7a to 7i show time-lag gathers as a function of the velocity error. The backscattered energy is still mapped vertically but away from $\tau = 0$. The backscattered events in the time-lag gathers show a kinematic error, i.e., these events move from positive τ for negative errors to negative τ values for positive errors. Figures 8a to 8i show a similar display for space-lag gathers. In this case, both backscattered energy and primary energy map away from $\lambda_x = 0$ when we introduce an error in the model. In space-lag gathers, the backscattered energy maps symmetrically away from zero lag with incorrect velocities. Finally, Figs. 9a to 9i show the sensitivity of CIPs to velocity errors. For incorrect velocity, the events move away from zero lags. In the CIPs, even when constructed with incorrect velocity, the primary reflections go through zero lag, and the events in the $\tau - \lambda_x$ plane show moveout (i.e., the energy not mapped symmetrically with respect to zero lag). The velocity errors split the backscattered energy in the $\lambda_z - \tau$ plane; some of the energy goes through zero space-lag while other part of the energy does not. We could use the information contained

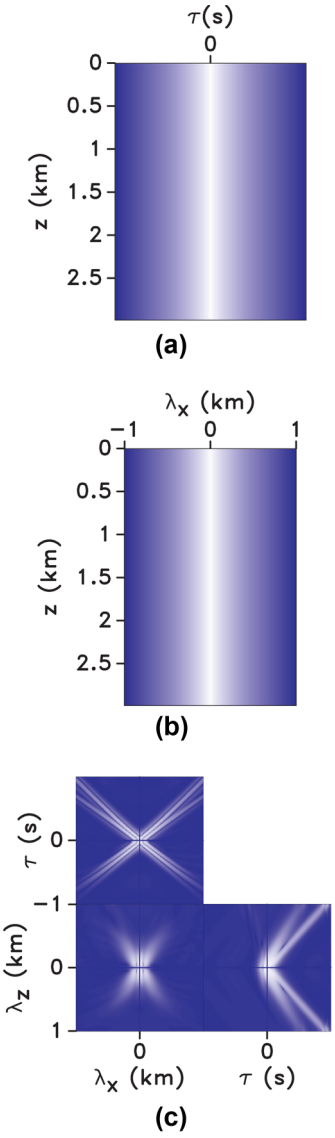


Figure 10 Penalty functions for (a) time-lag gathers, (b) space-lag gathers, (c) and CIP gathers. Blue and white colors represent low and high penalties, respectively.

in the extended images to design objective functions (OFs) that exploit the presence of backscattered events. Minimizing such OF, e.g., by wavefield tomography, optimizes the sharp interface positioning (e.g., the top of salt) and the sediment velocity above it. A straightforward approach based on differential semblance optimization (Shen, Symes, and Stolk 2003) can be adapted to use the backscattered energy seen away from zero lags by defining the OFs for time-lag gathers

$$J_\tau = \frac{1}{2}\|P(\tau)[R^{fb}(\mathbf{x}, \tau) + R^{bf}(\mathbf{x}, \tau)]\|_2^2, \tag{7}$$

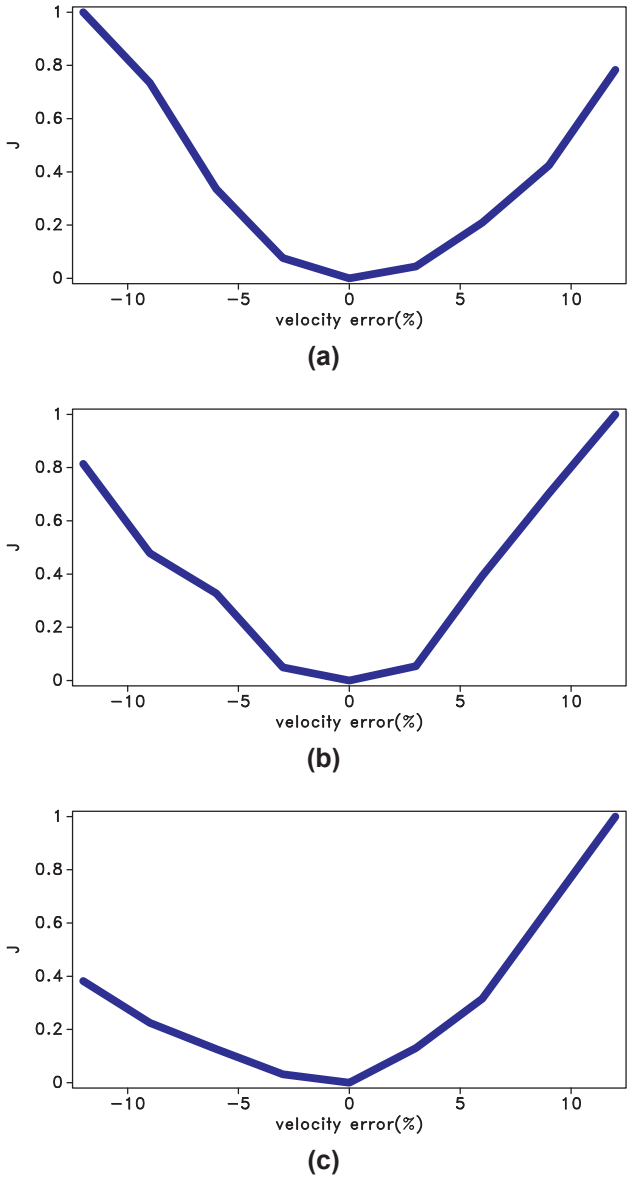


Figure 11 Normalized OFs for time-lag gathers: (a) J_τ, (b) space-lag gathers J_{λ_x}, and (c) CIP gathers J_c.

and for the space-lag gathers,

$$J_{\lambda_x} = \frac{1}{2} \| P(\lambda_x) \left[R^{fb}(\mathbf{x}, \lambda_x) + R^{bf}(\mathbf{x}, \lambda_x) \right] \|_2^2. \tag{8}$$

Here $P(\tau) = |\tau|$ and $P(\lambda_x) = |\lambda_x|$ are functions that penalize the backscattered energy away from zero lags, thus defining the residual that we need to minimize through inversion. For CIPs we can use the OF

$$J_c = \frac{1}{2} \| P(\lambda, \tau) [R^{fb}(\lambda, \tau) + R^{(}\boldsymbol{\lambda}, \tau)] \|_2^2. \tag{9}$$

Here, $P(\boldsymbol{\lambda}, \tau)$ is the penalty function for CIPs.

The penalty function is designed to measure the deviation or error between actual extended images and our notion for correct extended images. For CIGs we have a definite criterion. We know that the backscattered energy has to map to zero lag; that is why we can use the absolute value as a penalty function. However, for CIPs, the penalty operator is more complex. We use the correct CIP as reference for constructing the penalty function $P(\boldsymbol{\lambda}, \tau)$ similar to the one proposed by (Yang, Shragge, and Sava 2013). The correct CIP, shown in Fig. 1c, has the right focusing within the acquisition limitations. More generally, we could use a demigration/migration process to assess correct focusing at a given CIP position and to infer the shape of the penalty operator. *Once we obtain an image with the correct focusing for the current model, we can compute a penalty function such as*: $P(\boldsymbol{\lambda}, \tau) = \frac{E(R_c(\boldsymbol{\lambda}, \tau))}{<E(R_c(\boldsymbol{\lambda}, \tau)^2)> + \epsilon}$. *In this penalty function,* $E(.)$ *is the envelope of the image,* $< . >$ *is a smoothing operator, and* ϵ *is a stabilization factor.*

Figures 10a to 10c show the penalty functions for time-lag, space-lag, and CIP gathers, respectively. The OFs for our synthetic example are shown in Figs. 11a to 11c for time-lag gathers, space-lag gathers, and CIP gathers, respectively. One can see that, in all three cases, the OF minimizes at the correct model. If we want to optimize the model such that we maximize the backscattered events, we need to consider two variables: the velocity model and the interface geometry. In our example, the sharp interface depends linearly with the velocity model.

The OFs for CIGs are shown in Figs. 11a and 11b for time-lag gathers and space-lag gathers, respectively. One can see that the functions minimize at the correct velocity model. In the definition of the OF, we only use the backscattered energy $R^{fb}(z, \tau) + R^{bf}(z, \tau)$ and $R^{fb}(z, \lambda_x) + R^{bf}(z, \lambda_x)$ for time lag and space. We separate the wavefield contribution using wavefield up and down decomposition; alternatively, we could use slope filtering in the extended images. This is a robust and cost-effective operation since the various events in the gathers are characterized by distinct slopes, as shown by Kaelin and Carvajal (2011).

Examples

In this subsection we illustrate the backscattered events visible on extended images constructed based on a modified Sigsbee 2A model (Paffenholz *et al.* 2002). We modify the model by salt flooding (extending the salt to the bottom of the model) to avoid backscattering from the base of salt; therefore, we focus on the reflections from the top of salt only. For this

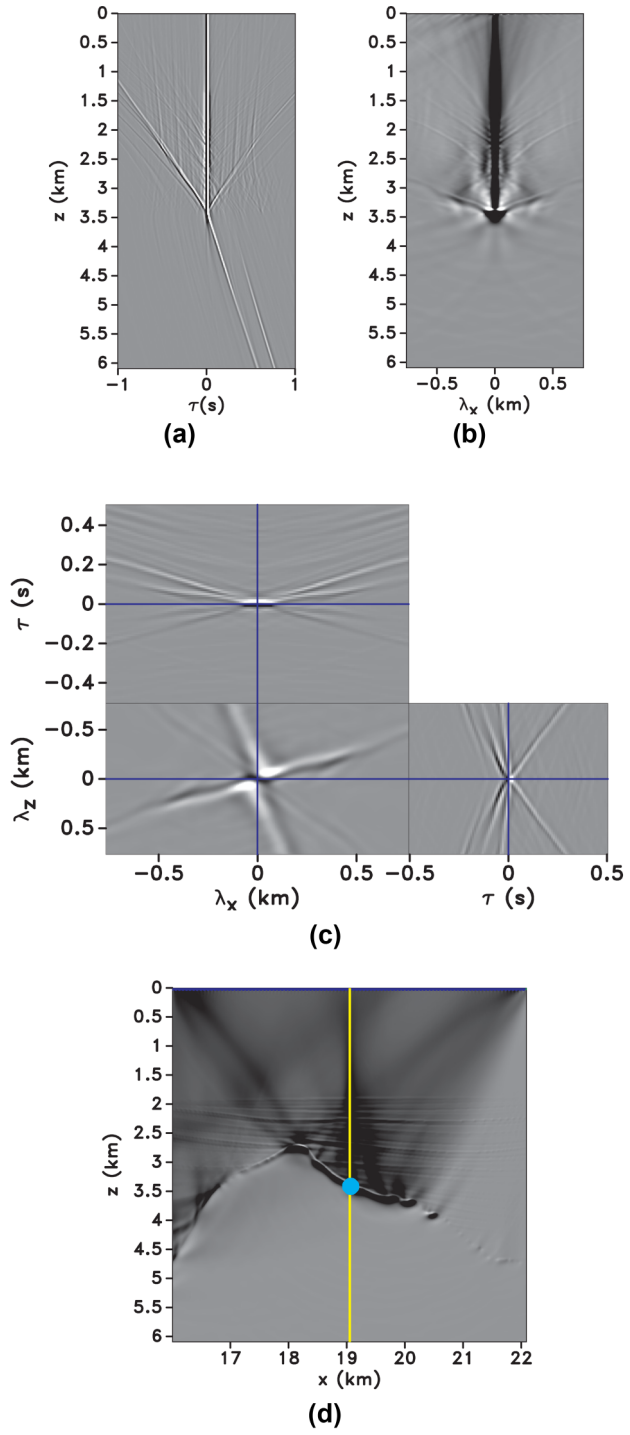


Figure 12 Sigsbee 2A analysis: (a) time-shift gather, (b) space-lag gather, (c) common image point, and (d) RTM image. The vertical line and thick point shown in the RTM image shows the CIG and CIP locations, respectively.

example we fix the receiver array on the surface, and we use 100 shots evenly sampled on the surface to build the image. For the migration model, we use the stratigraphic velocity, which shows sharp interfaces in the sediment subsection, in addition to the interface corresponding with the top of salt. Figure 12d shows the conventional image for our modified Sigsbee model; note the strong backscattered energy above the salt.

Figure 12a shows a time-lag gather calculated at $x = 19.05$ km. We can see that the gather is very complex, but we can easily identify the backscattered energy indicated with letter "a" in Fig. 1a. In this case, the backscattered energy maps directly to $\tau = 0$ because we use the correct velocity model. We can also identify the events corresponding to the cross-correlation between reflected waves from the source and receiver sides $R^{bb}(z, \tau)$, indicated with letter "b". The $R^{bb}(z, \tau)$ events have positive slope (given by the sediment velocity at the interface) and are visible for $\tau > 0$. We can also observe an abrupt change in the slope of the primary reflection corresponding the sediment–salt interfaces at the top of salt indicated with letter "c".

Figure 12b shows a space-lag CIG extracted at the same location. The backscattered energy maps toward $\lambda_x = 0$, indicated with letter "a". We see again the $R^{rr}(z, \lambda_x)$ case, indicated with letter "b", where the energy is mapped away from zero lag. Even though we are using the correct model, we still see energy away from $\lambda_x = 0$. This indicates that additional processing is needed before we can use space-lag gathers for model update with wave equation tomography.

Figure 12c shows a CIP extracted at the top of the salt interface at $(x, z) = (19.05, 3.4)$ km. Despite the complexity of this image, we can still identify similar patterns, as shown in Fig. 1c. The backscattered events are mapped to $\tau > 0$ in the $\tau - \lambda_z$ plane, indicated with letter "a". In this plane we can separate with the individual contributions from $R^{tr}(\mathbf{x}, \boldsymbol{\lambda}, \tau)$ (which maps to $\lambda_z < 0$ and $\tau > 0$) and $R^{rt}(\mathbf{x}, \boldsymbol{\lambda}, \tau)$ (which maps to $\lambda_z > 0$ and $\tau > 0$) because they are imaged into two different events, whereas in the CIGs previously discussed, we cannot differentiate the individual contributions because both cases map to zero lag. The image of the reflector maps as a point to zero lag in the $\tau - \lambda_x$ plane (indicated with letter "c").

Understanding the backscattered energy in the extended images for complex scenarios is the first step in using these events for MVA. In this article, we used wavefield decomposition to analyse the patterns of the backscattered energy in conventional and extended images. Although effective, wavefield decomposition can be very costly, epecially for 3D models.

In practice we need to use *slope* filtering of the extended images to isolate the events corresponding to the backscattered energy *(or the reflections)*.

CONCLUSIONS

Reverse time migration backscattered energy is produced by the correlation of waves originating at sharp boundaries (e.g., salt bodies) contained in the model. The two-way wave equation operator allows waves to travel in all directions for both the source and the receiver wavefields. Therefore, during the imaging condition (conventional or extended), we obtain events that contribute to the reflectivity and events that produce RTM backscattering for different source and receiver wavefield combination. The specific combinations that produce RTM backscattering indicate the synchronization between wavefields along the wavepaths that connect the source with the subsurface and the subsurface with the receivers. We have demonstrated that the RTM backscattered energy is sensitive to kinematic errors in the velocity model. Hence, a correct velocity model produces maximum synchronization or focusing along the incident and reflected wavepaths. The backscattered energy in the final image should not be considered as an artefact or a drawback of the imaging method; rather, the backscattered energy should be maximized in the image in order to ensure an optimum velocity model. The synchronization and focusing observations drawn in this paper demonstrate that the backscattering carries kinematic information that can be used during tomographic updates.

ACKNOWLEDGMENTS

The authors would like to thank the sponsors of the Center for Wave Phenomena, Colorado School of Mines, for their support. The numeric examples in this paper use the Madagascar open-source software package, freely available from *http://www.ahay.org*.

REFERENCES

Baysal E., Kosloff D.D. and Sherwood J.W.C. 1983. Reverse time migration. *Geophysics* **48**, 1514–1524.

Baysal E., Kosloff D.D. and Sherwood J.W.C. 1984. A two-way nonreflecting wave equation. *Geophysics* **49**, 132–141.

Claerbout J.F. 1985. Imaging the earth's interior. Blackwell Scientific Publications, Inc.

Fei T.W., Luo Y. and Schuster G.T. 2010. De-blending reverse-time migration. *SEG Technical Program Expanded Abstracts* **29**, 3130–3134.

Fletcher R.F., Fowler P., Kitchenside P. and Albertin U. 2005. Suppressing artifacts in prestack reverse time migration. *SEG Technical Program Expanded Abstracts* **24**, 2049–2051.

Gazdag J. 1978. Wave equation migration with the phase-shift method. *Geophysics* **43**, 1342–1351.

Gazdag J. and Sguazzero P. 1984. Migration of seismic data by phase shift plus interpolation. *Geophysics* **49**, 124–131.

Guitton A., Kaelin B. and Biondi B. 2007. Least-squares attenuation of reverse-time-migration artifacts. *Geophysics* **72**, S19–S23.

Kaelin B. and Carvajal C. 2011. Eliminating imaging artifacts in rtm using pre-stack gathers. *SEG Technical Program Expanded Abstracts* **30**, 3125–3129.

Liu F., Zhang G., Morton S.A. and Leveille J.P. 2011. An effective imaging condition for reverse-time migration using wavefield decomposition. *Geophysics* **76**, S29–S39.

McMechan G.A. 1983. Migration by extrapolation of time-dependent boundary values. *Geophysical Prospecting* **31**, 413–420.

Paffenholz J., McLain B., Zaske J. and Keliher P. 2002. Subsalt multiple attenuation and imaging: Observations from the Sigsbee 2B synthetic dataset. dataset. 72nd SEG annual international meeting, Expanded Abstracts, 2122–2125.

Rickett J.E. and Sava P.C. 2002. Offset and angle-domain common image-point gathers for shot-profile migration. *Geophysics* **67**, 883–889.

Sava P. and Fomel S. 2006. Time-shift imaging condition in seismic migration. *Geophysics* **71**, S209–S217.

Sava P. and Vasconcelos I. 2011. Extended imaging conditions for wave-equation migration. *Geophysical Prospecting* **59**, 35–55.

Sava P. and Vlad I. 2011. Wide-azimuth angle gathers for wave-equation migration. *Geophysics* **76**, S131–S141.

Sava P.C. and Fomel S. 2003. Angle-domain common-image gathers by wavefield continuation methods. *Geophysics* **68**, 1065–1074.

Shen P., Symes W.W. and Stolk C.C. 2003. Differential semblance velocity analysis by wave-equation migration. *SEG Technical Program Expanded Abstracts* **22**, 2132–2135.

Whitmore N.D. 1983. Iterative depth migration by backward time propagation. *SEG Technical Program Expanded Abstracts* **2**, 382–385.

Yang T. and Sava P. 2010. Moveout analysis of wave-equation extended images. *Geophysics* **75**, S151–S161.

Yang T., Shragge J. and Sava P. 2013. Illumination compensation for image-domain wavefield tomography. *Gephysics* **78**, U65–U76.

Youn O.K. and Zhou H. 2001. Depth imaging with multiples. *Geophysics* **66**, 246–255.